Dalton Transactions

ROYAL SOCIETY OF CHEMISTRY

PAPER

View Article Online
View Journal | View Issue

Check for updates

Cite this: *Dalton Trans.*, 2025, **54**, 14547

Structural and magnetic properties of mixed-metal $(Bi_2O_2)(Fe_{1-x}M_xF_4)$ Aurivillius oxyfluorides

Jonas Wolber, [a,b] Victor Duffort, [a] Claire Minaud, [a] Marielle Huvé, [a] Mathieu Duttine, [c] Ángel-M. Arévalo-López, [a] Oscar Fabelo, [b] Clemens Ritter [b] and Olivier Mentré *[a]

A series of mixed-metal Aurivillius oxyfluorides of the ideal formula $[Bi_2O_2][Fe_{1-x}M_xF_4]$ was synthesized by hydrothermal synthesis with M = Mn, Co, and Ni. We first re-examined the Fe-only compound and deduced that despite the observation of inhomogeneous lattice parameters between batches, the iron valence remains constant around $Fe^{\sim 2.5+}$ in all samples measured using Mössbauer spectroscopy. The mixed valency charge compensation is mainly assigned to the formation of Bi vacancies. For the mixed Fe/M phases, the most common observation, using various diffraction techniques, of long-range ordering between tilted $[(Fe,M)F_6]$ octahedra in the perovskite layers is reminiscent of the Fe, Co, and Ni parent members. This validates the possibility of well-defined anion-ordering, despite the mixing of cations with different ionic radii. A qualitative matching between the lattice evolution along the Fe/M solid solutions and our DFT relaxed ideal models supports this idea. Differences in the magnetic structures are observed between the single-metal and the mixed Fe/M compositions, while retaining ordered magnetic structures and escaping spin-glass behavior despite disordered Fe/M ions. In contrast to the non-collinear antiferromagnetic spin arrangements obtained in most of the parent cases, the majority of the mixed Fe/M compounds show a collinear structure with spins aligned along the *c*-axis, similar to the single-metal M = Mn^{2+} (L = 0) case in which spin–orbit coupling is absent. This suggests the predominant role of the spin contribution to the ordering of the magnetic moments as soon as both Fe and M intervene.

Received 3rd June 2025,
Accepted 18th August 2025

DOI: 10.1039/d5dt01303h

rsc.li/dalton

Open Access Article. Published on 22 Liiqen 2025. Downloaded on 09/12/2025 6:56:30 AM.
This article is licensed under a Creative Commons Attribution-NonCommercial 3.0 Unported Licence.

Introduction

As a general principle, the oxyfluoride structural edifices exhibit more ionic M–F bonds and more covalent M–O bonds due to the superior charge and polarizability of the oxide anions. In this regard, the Aurivillius oxyfluorides emerge as intriguing modifications of their parent layered ferroelectric oxides. Indeed, starting from their modular developed formula, $(Bi_2O_2)_{fluorite}(A_{n-1}M_nO_{3n+1})_{perovskite}$, the incorporation of F^- anions in the perovskite slabs enables the stabilization of stoichiometric n = 1 members with M transition metals in an oxidation state lower than +6, usually found in the well-known $(Bi_2O_2)(M^{6+}O_4)$, M = Mo, W oxides. This leads to phases such as $(Bi_2O_2)((Nb/Ta/V)^{5+}O_3F)$ and $(Bi_2O_2)(Ti^{4+}O_2F_2)$,[1–3] in which the ferroelectricity is ambiguous due to the combination of O/F mixed and split positions.[3–7] Surprisingly, an antiferroelectric behavior, *i.e.*, transitioning from a non-polar to a polar phase under an electric field, was recently demonstrated for $(Bi_2O_2)(Ti^{4+}O_2F_2)$. This structural change is governed by an original mechanism involving the rotation of the $[TiO_3F_3]$ octahedra within the perovskite layers. The resulting shifts of O^{2-} and F^- ions along the *c*-axis are often different in magnitude and correlated with their different valences.[7]

This aspect further highlights the broad range of interest in the heteroleptic coordination of transition metal centers. Another significant step forward was achieved by the preparation of n = 1 Aurivillius oxyfluorides with the ideal formula $(Bi_2O_2)(M^{2+}F_4)$ containing paramagnetic $3d^n$ transition metal ions M = Fe, Co, Ni, and Mn.[8–11] Their structural features range from disordered average cells to anionic-ordered supercells, and their magnetic structure evolves from collinear to canted magnetic spin orientations, depending on the electronic configuration of the metal ion. For instance, the combination of a canted spin structure and a polar nuclear superstructure allows for multiferroicity in the M = Fe case.[8] Conversely, the M = Mn^{2+} (d^5) case reveals structural disorder between F^- anions, resulting from various equiprobable arrangements between tilted $[MnF_6]$ octahedra due to their

[a]*UCCS (Unité de Catalyse et Chimie du Solide) – Axe Chimie du Solide, UMR-CNRS 8181, Ecole Centrale/Université de Lille, F-59655 Villeneuve d'Ascq, France. E-mail: olivier.mentre@univ-lille.fr*
[b]*ILL (Institut Laue-Langevin), F-38042 Grenoble, France*
[c]*CNRS, Université de Bordeaux, Bordeaux INP (Institut Polytechnique de Bordeaux), ICMCB (Institut de Chimie de la Matière Condensée de Bordeaux), UMR 5026, F-33600 Pessac, France*

Open Access Article. Published on 22 Liiqen 2025. Downloaded on 09/12/2025 6:56:30 AM.
This article is licensed under a Creative Commons Attribution-NonCommercial 3.0 Unported Licence.

low-energy crystal field distortion modes and possible lattice defects.[11] Combining two transition metals within the perovskite structure is also an effective approach to modify the magnetic properties while tuning/inducing functional properties. For instance, $YFeO_3$ [12] and $YCrO_3$ [13] exhibit canted antiferromagnetic ordering around 640 K and 140 K, respectively. In contrast, $YFe_{0.5}Cr_{0.5}O_3$ shows magnetization reversal with a high compensation temperature.[14] In this context, the synthesis and investigation of mixed-metal $(Bi_2O_2)(Fe_{1-x}M_xF_4)$ emerges as an interesting method to enforce octahedral disorder and to evaluate the impact on the lattice. Here we first re-examine the Fe compound with evidence of significant variations of lattice parameters and Fe oxidation states, due to hardly-controllable defects even for a single targeted ideal $(Bi_2O_2)(FeF_4)$ composition. Then, we investigate the Fe/M solubility for M = Mn, Co, and Ni in the Aurivillius oxyfluorides. Special attention was paid to the dispersion of the lattice parameters for similar targeted Fe/M composition, which suggests the onset of various lattice defects including Bi vacancies, like those present in the single-metal M = Fe case.[8] As expected in 2D mixed-cation systems, both the Fe/M random distribution and the overlap between the Fe/M 3d levels with shifted energies mediated by hybridized anionic ligands are expected to create high structural (anionic) and magnetic disorder. This was investigated by means of electron diffraction, neutron diffraction and X-ray powder diffraction, and magnetic measurements, together with DFT calculations.

Experimental

Synthesis of the mixed Fe/M Aurivillius phases

The samples were prepared by hydrothermal synthesis in Parr general purpose acid digestion vessels 4749 with A280AC 23 mL Teflon liners. For a typical synthesis of 2 g batches, 12 drops of hydrofluoric acid (40%) were diluted in 10 mL of deionized water. The transition metal fluorides were weighed in an argon filled glovebox and ground with bismuth(III) oxide (previously decarbonized at 600 °C for 12 h) under open air conditions before adding them to the acidic solution. The closed vessels were heated for 3 h up to 230 °C, kept at this temperature for 72 h, and cooled down to 25 °C in 1 h. The product was filtered, washed with deionized water and ethanol, and dried at 100 °C for approximately 1 h. Many variations of this protocol were tested to increase sample purity of the targeted composition of $Bi_2O_2FeF_4$, resulting in the cell parameter distribution shown in Fig. 1a. Detailed reactant quantities, temperature profiles, water volumes, *etc.* are extensively listed in Tables S2–S5. In Table S1, we also report the wt% of each phases identified and quantified by XRD-Rietveld refinements for all samples measured magnetically and/or by neutron powder diffraction (NPD).

The ratios of FeF_2 (Alfa Aesar, 98%), MF_2 (CoF_2 Alfa Aesar 99.99%, NiF_2 Thermo Scientific 97%, MnF_2 Sigma Aldrich 98%), and Bi_2O_3 (Johnson Matthey Chemicals Limited 99.9%) were optimized through trial and error to minimize impurities. Overall, $BiO_{0.5}F_2$, BiOF, and $Bi_7F_{11}O_5$ side products are obtained on the bismuth-rich side and Fe_2O_3, FeF_2, FeF_3, $Fe_2F_5(H_2O)_x$, $FeO_{0.3}(OH)_{0.7}(H_2O)_{0.175}F$, and most likely mixed-metal compositions of those compounds not yet reported in the literature are obtained when working with an excess of the transition metals. Perfect ratios could not be achieved as both bismuth and transition metal impurities are observed close to the optimized ratios, most likely due to the decreasing solubilities of the fluorides in hydrofluoric acid during the cool-down to room temperature. This leads to the precipitation of impurity rich phases essentially on top of the targeted product. For this reason, the top layer was systematically removed, to increase purity, but all samples still contain sizable amounts of impurities, sometimes visible in magnetic measurements

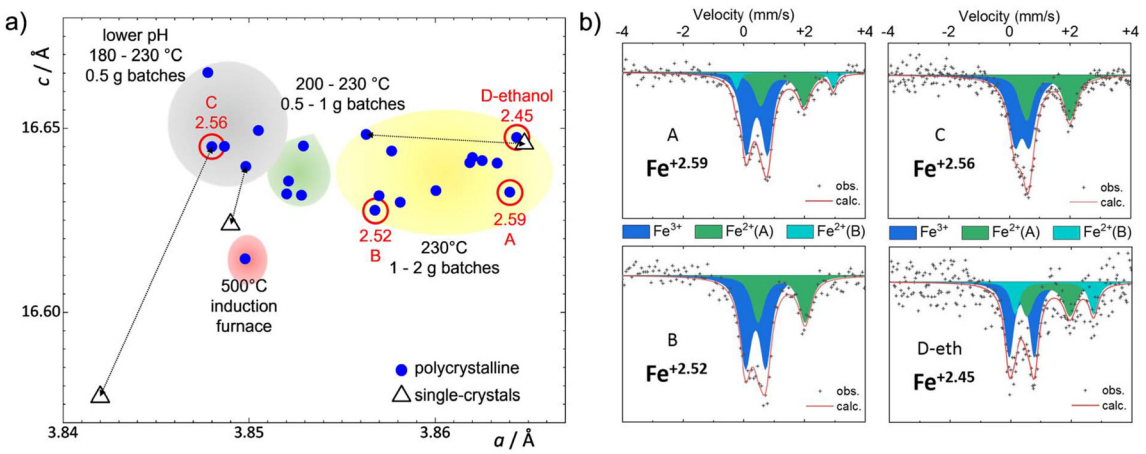

Fig. 1 $Bi_{2-x}O_2FeF_4$. (a) Lattice parameters *a vs. c* obtained by Rietveld refinement in the average high symmetry *I*4/*mmm* cell for different polycrystalline sample batches. Variations of *a* can be understood as intra-layer and changes along *c* as inter layer effects. Triangles give lattice parameters derived from single crystals picked out of the connected batches. Red circles indicate samples analyzed using Mössbauer spectroscopy and colored areas are used to cluster specific synthesis conditions. (b) ^{57}Fe Mössbauer spectra (293 K) of four different batches: A, B, C, D (see the text for details).

This journal is © The Royal Society of Chemistry 2025

Open Access Article. Published on 22 Liiqen 2025. Downloaded on 09/12/2025 6:56:30 AM. This article is licensed under a Creative Commons Attribution-NonCommercial 3.0 Unported Licence.

and neutron diffractograms. This precipitation cannot be avoided since the reaction vessels cannot be opened at high temperature.

Technical details

XRPD. Room temperature X-ray powder diffraction (XRPD) was carried out using a Bruker D8 Advance in Bragg–Brentano geometry (Cu-K_α).

NPD. Low temperature neutron powder diffraction (NPD) patterns were recorded on the D1B (λ = 2.52 Å) diffractometer at Institut Laue-Langevin (ILL) in Grenoble. Additional high resolution room temperature data were obtained using the high-resolution diffractometer D2B (λ = 1.59 Å).

Data analysis and presentation. Rietveld refinements of the powder data were carried out using Fullprof (V7.30).[15] Irreducible representations were taken from BasIReps, and the Shubnikov groups were determined from the generated .mcif file using the ISOCIF tool of the ISOTROPY Suite.[16] Plots were created in Origin 2021b. Pictures of crystal structures were prepared in Diamond (V4.5.1).

Magnetic measurements. Magnetic measurements were carried out on a Quantum Design PPMS 9T DynaCool magnetometer. For zero field cooled (ZFC) measurements, the samples were cooled down to 1.5 K without an external magnetic field and the data were recorded on heating in an external field of 0.1 T. The field cooled (FC) data were then recorded in the same external field on cooling.

Mössbauer spectroscopy. ^{57}Fe Mössbauer spectra were recorded in transmission with constant acceleration in a Halder-type spectrometer equipped with a ^{57}Co(Rh) source (1.5 GBq). The ^{57}Fe isomer shifts are referenced to room temperature α-Fe^0. The Mössbauer hyperfine parameters (isomeric shift δ, quadrupole splitting Δ, Lorentzian line width Γ, and relative area) were refined using homemade programs and WinNormos.[17]

TEM. A FEI Tecnai G2-20 twin (200 kV) transmission electron microscope (TEM) was used to do selected area electron diffraction (SAED, or short ED) combined with EDX analysis on selected particles of the powders. Energy dispersive X-ray spectroscopy (EDX) permits elemental analysis. The powder was prepared in the form of an alcohol suspension dropped on carbon supported copper grids followed by evaporation of the alcohol under ambient conditions.

DFT calculations. Theoretical calculations were performed using density functional theory (DFT) within the Vienna *ab initio* simulation package (VASP).[18–20] The generalized gradient approximation (GGA) with Perdew–Burke–Ernzerhof (PBE) functional was employed for electron exchange and correlation.[21] Atom cores were described through the projector augmented wave (PAW) method.[22] The kinetic energy cutoff for plane wave expansions was set to 400 eV for all calculations. Atomic positions were optimized until forces were converged to lower than 10^{-3} eV Å^{-1}. A Hubbard U correction was added using the GGA+U method[23] with $U_{\text{eff}} = U - J = 4$ eV. The electronic convergence criterion of 10^{-8} was used. We used the ~5.5 Å, ~5.5 Å, ~16.5 Å cell and a 4 × 4 × 2 Monkhorst–Pack mesh for the Brillouin zone sampling.[24] For the magnetic exchanges, we used similar spin-polarized Heisenberg models as used in our former works on Fe, Ni, and Mn.[8,11]

Results and discussion

Fe valence and lattice flexibility in $(Bi_{2-x}O_2)(FeF_4)$

The underlying reason for the preparation of mixed Fe/M phases is the prior experimental evidence of magneto-electric coupling at T_N, canted antiferromagnetic ordering, and electric polarization loops in $(Bi_{2-x}O_2)(FeF_4)$, the typical signatures of multiferroics.[25] Therefore, prior to the investigation of the mixed phases, we re-examined the parent Fe compound complementing our initial work. Structurally, the Aurivillius oxyfluoride phases considered here ideally consist of the stacking of fluorite $(Bi_2O_2)^{2+}$ and $(M^{2+}F_4)^{2-}$ perovskite blocks. However, in our initial study we reported that the iron valence was significantly shifted higher than its ideal Fe^{2+} valence, up to $Fe^{\sim 2.5+}$. This deviation is compensated by the formation of ~10% of Bi vacancies, as refined from single crystal XRD data, while keeping the ideal $[FeF_4]$ formula for the perovskite units.[8] Moreover, in our recent investigation of the M = Mn compound,[11] other plausible lattice defects emerged from electron microscopy annular dark-field imaging and thermal analyses, such as O ↔ F antisite disorder or substitutions combined, or not, with Bi vacancies. These defects might also, to a lower extent, be present in the Fe case impacting lattice constants and other structural characteristics.

Therefore, while accurate investigation of such defects by theoretical calculations is beyond the scope of this paper, we looked for correlation between the synthesis conditions and the a and c lattice parameters of the average ($I4/mmm$) cell, refined from XRD data (Fig. 1a and Table S2). For four of these samples, the iron valence was determined using Mössbauer spectroscopy (see Fig. 1b and Table 1 for experimental and fitting details). Experimentally, samples A and B were prepared as explained above for "standard" samples while sample C was prepared for a lower total amount of precursors (~0.5 g). For

Table 1 $Bi_{2-x}O_2FeF_4$. Refined ^{57}Fe Mössbauer hyperfine parameters (isomeric shift δ, quadrupole splitting Δ, and line width Γ) from room temperature (293 K) measurements on four different batches of $Bi_{2-x}O_2FeF_4$. Batch B was included in a previous publication.[8] The oxidation states are given after correction by the Lamb Mössbauer factors reported in the text

Batch	Species	δ/mm s^{-1}	Δ/mm s^{-1}	Γ/mm s^{-1}	Area/%	Ox-state
A	Fe^{3+}(A)	0.44(3)	0.69(4)	0.41(5)	61(5)	+2.59
	Fe^{2+}(A)	1.27(6)	1.45(8)	0.49(7)	31(5)	
	Fe^{2+}(B)	1.36(7)	3.19(8)	0.24(7)	8(5)	
B	Fe^{3+}(A)	0.43(3)	0.48(5)	0.49(3)	59(3)	+2.52
	Fe^{2+}(A)	1.29(3)	1.46(6)	0.47(5)	41(3)	
C	Fe^{3+}(A)	0.40(3)	0.67(4)	0.44(5)	63(5)	+2.56
	Fe^{2+}(A)	1.25(5)	1.55(6)	0.46(5)	37(5)	
D-eth	Fe^{3+}(A)	0.37(3)	0.8(1)	0.35(9)	47(5)	+2.45
	Fe^{2+}(A)	1.25(8)	1.4(2)	0.50(—)	31(5)	
	Fe^{2+}(B)	1.44(8)	2.6(2)	0.40(—)	22(5)	

Open Access Article. Published on 22 Liiqen 2025. Downloaded on 09/12/2025 6:56:30 AM.
This article is licensed under a Creative Commons Attribution-NonCommercial 3.0 Unported Licence.

sample D, the solvothermal treatment was achieved in a 50–50 mixture of ethanol and deionized water. Their XRD patterns are shown in Fig. S1. The main goal of this preliminary study before mixing Fe/M cations was to probe divergences between batches with the same targeted compositions. For all samples, we found two main components: Fe^{2+}(A) and Fe^{3+}(A) intrinsic to the major Aurivillius phase. In two of the four samples examined using Mössbauer spectroscopy (samples A and D), we also found an Fe^{2+}(B) contribution, whose fitted parameters approach those of $Fe(OH)_2$ and FeF_2.[26–28] This secondary phase contribution was not properly assigned by XRD. The average Fe oxidation numbers given in Table 1 were calculated from the Fe^{3+}–Fe^{2+} relative proportions that were corrected considering the Lamb–Mössbauer factors (f) of Fe^{3+} (0.77) and Fe^{2+} (0.57) at 293 K (f factors were estimated from low-temperature measurements performed on batch C).

On average, we observe a weak dispersion of the lattice parameters (~0.4% along a, ~0.3% along c) on polycrystalline samples which could arise from defects, but also from microstructural features possibly systematically influencing anisotropically the lattice; and/or incorporation of water molecules either blocking the crystal growth during the synthesis but also possibly during the preparation of the powder XRD samples. This latter possibility is further supported by the important variation of lattice parameters measured on single crystals and powder XRD from the same batches (see the black dotted arrows in Fig. 1a). It is difficult to further rationalize this aspect. In addition, Mössbauer data show a narrow distribution of iron valences from +2.45 to +2.59 measured on samples with various lattice parameters. The oxidation state of iron seems rather homogeneous considering the inaccuracies due to the poor statistics, even after 3 weeks of signal accumulation, due to the strong absorption of bismuth. Importantly, the variability observed in the a parameter is not correlated to the valence state of iron. Hence, the ~10% cationic vacancies balancing the presence of Fe^{3+} in $(Bi_{1.8}O_2)(Fe^{+2.6}F_4)$, previously observed from both NPD and single crystal XRD data,[8] are not the main reason for the distribution of the cell parameters. It strongly suggests the occurrence of additional defects.

The analysis of Mössbauer spectra of four selected batches shows a medium distribution of isomeric shifts (δ) and the quadrupolar splitting (Δ) parameters for both the intrinsic Fe^{2+} (δ: 1.25–1.29; Δ: 1.4–1.55) and Fe^{3+} (δ: 0.37–0.44; Δ: 0.48–0.8) contributions. This validates significantly covalent Fe–F bonding, in agreement with the rather regular $[FeF_6]$ units and short octahedral bond distances between 1.83 Å and 2.20 Å reported in a previous publication.[8] Full widths at half maximum (FWHM, Γ) of the Mössbauer resonance lines suggest a certain degree of disorder, on average, compatible with the existence of local defects.

Octahedral-tilt ordering in the single-metal parent phases

Despite the lattice variations being prominent in the Fe-phases, and also observed to a lower extent in various batches of single-metal phases with M = Mn, Co, Ni, some features of the diffraction pattern are specific to each metal. For instance, in our previous investigation of $(Bi_2O_2)(MnF_4)$[11] the selected area electron diffraction (SAED) patterns show mainly the ideal $I4/mmm$ disordered subcell ($a_p = b_p \sim 3.8$ Å, $c \sim 16.5$ Å, where the p indices denote the analogy with perovskites) as shown Fig. 2a. These patterns are complicated by various long-range-ordering supercell features for M = Fe, Co, and Ni compounds (Fig. 2b–d) due to the cooperative combinations of equatorial and axial tilts of the $[MF_6]$ octahedra in the perovskite layers. It reduces the symmetry from tetragonal to an orthorhombic ($\sqrt{2}\cdot a_p$, $\sqrt{2}\cdot b_p$, c) supercell; this orthorhombic orientation is used to index all the ED patterns of Fig. 2. In the three concerned compounds, *e.g.*, M = Fe, Co, Ni, the polar $P2_1ab$ symmetry was reported.[8–10] The orthorhombic supercell spots are indicated by red arrows on Fig. 2.

Extra phenomena (systematic or not) observed due to more local-to-medium range ordering are sometimes observed depending on the nature of the M cation, as shown by white arrows in Fig. 2a–d. For instance, for M = Fe we found a commensurate propagation vector $\mathbf{q} = (0, \frac{1}{2}, 0)$ related to the orthorhombic double cell.[8] It was also detected in single crystals and refined to in-plane antipolar displacements of the Fe atoms. For M = Co and Ni, weak modulation vectors were detected with $\mathbf{q} = (\frac{1}{2}, \frac{1}{2}, 0)$ and (0.48, 0.48, 0) respectively. These latter modulation vectors are not observed in XRPD/NPD patterns.[8,9] In the next section, we examine how these ED features evolve in the mixed Fe/M compounds.

Fine structural features in the mixed Fe/M phases

After checking by XRD that the as-prepared mixed-metal compounds correspond to a single Aurivillius phase, we first present their typical electron diffraction (ED) characteristics, with a special focus on the mixed Fe/Co series. Here, dealing with rather different cationic sizes and amplitudes of the octahedral tilting, it is interesting to probe how the long-range ordering could be developed. Intuitively, one could expect the loss of the ordering specific to one metallic center with increasing substitution, resulting in an average subcell similar to the M = Mn case. We recall in this case that the lack of octahedral ordering in the (MnF_4) layers mainly stems from favorable local $[MnF_6]$ distortions, allowed by the flexible d^5 crystal field.[11] Fig. 2e–j show the ED patterns taken along the [−110] zone axis, for several Fe/M ratios. The announced compositions were determined from averaging the EDX results on several crystals within the same batch. Here only the most representative patterns are displayed, but slight variations in the Bi/Fe/M compositions (from *in situ* EDX analysis) and of the intensities of the supercell-spots were detected within each batch, as highlighted between Fig. 2f and g dealing with a single $Fe_{\sim 0.6}Co_{\sim 0.4}$ batch. At least we can conclude that for the Fe/Co mixed-metal compounds (Fig. 2e–h) the orthorhombic supercell spots are preserved for Fe-rich compositions and "*sometimes lost*" for Co-rich ones. To a first approximation, the ED emphasizes the collaborative tilting of $[FeF_6]$ and $[CoF_6]$ octahedra in the perovskite layers. However, due to some pattern and compositional variations, these also indicate sample inhomogeneities at least on the examined thin areas

 This journal is © The Royal Society of Chemistry 2025

Open Access Article. Published on 22 Liiqen 2025. Downloaded on 09/12/2025 6:56:30 AM.
This article is licensed under a Creative Commons Attribution-NonCommercial 3.0 Unported Licence.

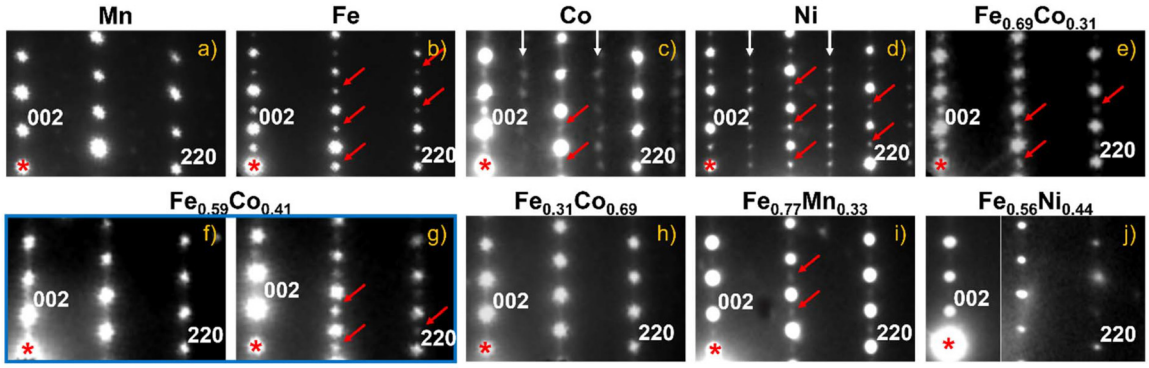

Fig. 2 $Bi_2O_2(M,M')F_4$. Electron diffraction on different prepared samples recorded along the [–110] zone axis referred to as the $\sqrt{2}\cdot a_p$, $\sqrt{2}\cdot b_p$, c supercell. (a) Mn given for comparisson does not show any supercell spots. (b–i) Red arrows indicate spots assigned to $P2_1ab$ lattice ordering by cooperative octahedral tilting in the perovskite layers. For Ni and Co (c) and (d), the white arrows show extra phenomena discussed in the text. The announced Fe/M stoichiometry (e)–(j) was determined by averaging the EDX analysis on various crystallites of the same corresponding batches. For (j) the contrast has been adapted for the right part of the image.

(crystal edges), possible local high defect concentration and/or specific local Fe/Co distribution preventing coherent octahedral tilts over long distances. Similarly, very weak or absent modulation spots have been observed in the $Fe_{0.56}/Ni_{0.44}$ (Fig. 2j) and $Fe_{0.77}/Mn_{0.33}$ (Fig. 2i) sample, which is not surprising in the latter case with respect to the fully disordered parent Mn-phase.[11] Here one can assume that both the distortion of $[MnF_6]$ octahedra allowed for d^5 ions and the large Fe/Mn difference of ionic radii are major drawbacks for developing perfect long-range ordering along the $Fe_{1-x}Mn_x$ solid solution. These effects are expected much lower in the $Fe_{1-x}Co_x$ mixed systems.

We never observed evidence for the additional (in)commensurate modulation discussed above in the mixed-metal compounds. This highlights that the involved fine structural details are fragile and destroyed by the Fe/M random cationic disorder.

Diffraction clues for the collaborative octahedral tilting were also examined by powder XRD. In this context, Fig. 3 shows clear evidence of the long-range orthorhombic ordering in the parent Fe phase and in the mixed Fe/Co phases, as indicated by (*) on the concerned peaks. However, increasing the Co content slightly broadens and weakens these XRD peaks, sometimes hidden by the contribution of secondary phases. It is in tune with our ED investigation. In the mixed Fe/Ni case, our XRD data look even more ambiguous but reveal some broad indications of the $\sqrt{2}\cdot a_p$, $\sqrt{2}\cdot b_p$, c supercell, not observed on ED. Here again, some sample inhomogeneities between thin crystal areas and the bulk can be deduced. For mixed Fe/Mn compounds, the two examined samples might lack the orthorhombic symmetry completely but significant amount of impurities limit our deep investigation. Overall, the XRD results are consistent with the previously discussed ED, which shows only weak (Fe/Mn) to extremely weak (Fe/Ni) supercell reflection spots probing the more local behavior on single particles. At the submicronic coherence length typical of XRD, the powder diffractograms may confirm that the large difference of ionic radii between the Fe/Mn and Fe/Ni pairs

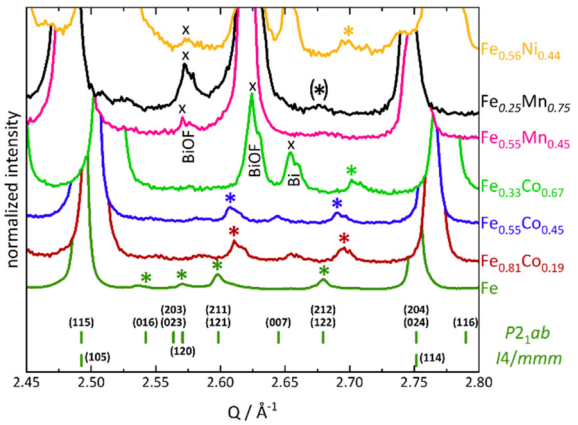

Fig. 3 $Bi_2O_2Fe_{1-x}M_xF_4$. Part of the XRD patterns (Cu-K_α) of different Fe/M compositions. The Q range is selected to show supercell reflections of the $P2_1ab$ space group with minimal overlap of impurities. Supercell reflections are marked with *a* * and impurities with an *x*. The composition is determined by NPD or EDX and sometimes assumed from the synthesis (italic). The diffraction pattern of the pure Fe phase is recorded in the ERSF (ID31, λ = 0.1652 Å).

could quench the long-range tilt ordering, while the closer Fe/Co ionic radii preserve the cooperative distortion. Our neutron diffraction experiments, described below, should be more sensitive than XRD to the distortions of the anionic sublattice. Unfortunately, due to the instrumental resolution and the presence of impurities that give a non-negligible peak overlap, this benefit was not fully exploited.

Computational study of the structural relaxation of Fe, M, and mixed Fe/M compounds

In order to check the "expected" lattice evolution on M^{2+} for Fe^{2+} substitution, we first performed full structural relaxation for M = Mn, Fe, Co, and Ni using GGA+U, starting from the centrosymmetric *Pcab* (61) models (adding an inversion center to $P2_1ab$ (29)). Details are given in the Technical details

Open Access Article. Published on 22 Liiqen 2025. Downloaded on 09/12/2025 6:56:30 AM.
This article is licensed under a Creative Commons Attribution-NonCommercial 3.0 Unported Licence.

Table 2 $Bi_2O_2(M,M')F_4$. DFT+U relaxed structures and calculated magnetic exchange parameters J in between neighboring magnetic cations' intra- and interlayers as well as the calculated magnetic moments on the cation centers. The M–F–M angles give a measure of the octahedral tilt in the perovskite layers (see Fig. 5b). Ionic radii are given for high spin 6-fold coordination and averaged for the mixed compositions.[29] 'Not converged' magnetic exchanges show that some of the three configurations did not energetically converge after 200 cycles

Compound $r_{ion,M.}$ (Å)	Lattice param. (Å)	∠M–F–M	V (Å^3)	Fe–F/M–F (Å)	J_{intra}/J_{inter} ($K{\cdot}k_B$) +:AFM, −:FM	M_{Fe}/M_M (μ_B per ion)
$(Bi_2O_2)(MnF_4)$	5.45 90.00	133°/133°	484.75	Mn–F = 2.08–2.10	+5.83/+0.01	M_{Mn} = 4.69
0.83	5.40 90.00					
	16.47 90.00					
$(Bi_2O_2)(FeF_4)$	5.42 90.00	138°/138°	475.92	Fe–F = 2.01–2.07	+10.83/+0.01	M_{Fe} = 3.80
0.78	5.37 90.00					
	16.34 90.00					
$(Bi_2O_2)(CoF_4)$	5.41 90.06	141°/141°	469.42	Co–F = 2.02	Calc. FM	M_{Co} = 2.81
0.745	5.37 90.00					
	16.18 90.00					
$(Bi_2O_2)(NiF_4)$	5.39 90.00	144°/144°	462.37	Ni–F = 1.97–2.00	+86.49/+0.04	M_{Ni} = 1.80
0.69	5.36 90.00					
	16.00 90.00					
$(Bi_2O_2)(Fe_{\frac{1}{2}}Mn_{\frac{1}{2}}F_4)$	5.44 90.00	133°/138°	480.47	Fe–F = 2.01–2.07	+8.69/+0.01	M_{Fe} = 3.80
0.805	5.39 89.90					M_{Mn} = 4.69
	16.41 90.00			Mn–F = 2.08–2.10		
$(Bi_2O_2)(Fe_{\frac{1}{2}}Co_{\frac{1}{2}}F_4)$	5.42 90.00	137°/142°	472.89	Fe–F = 2.01–2.07	Not converged	—
0.763	5.37 89.75					
	16.25 90.00			Co–F = 2.02		
$(Bi_2O_2)(Fe_{\frac{1}{2}}Ni_{\frac{1}{2}}F_4)$	5.41 90.00	138°/145°	469.51	Fe–F = 2.01–2.08	Not converged	M_{Fe} = 3.84
0.735	5.37 89.68					M_{Ni} = 1.78
	16.17 90.00			Ni–F = 1.98–2.00		

section. We also built and relaxed ideal in-plane Fe/M ordered structures corresponding to the $(Bi_2O_2)(Fe_{\frac{1}{2}}M_{\frac{1}{2}}F_4)$ compounds such that each M metallic center is surrounded by four Fe atoms. Here, the initial symmetry is lowered from *Pcab* (61) to monoclinic $P2_1/c11$ (14). All structures converged into slightly distorted triclinic unit cells. The relaxed lattice parameters and the main M–F distances are listed in Table 2.

For the single-metal cations, the average in-plane (a, b) and c parameters evolve following the average metal ionic radii. They are given in Table 2 for the high-spin configurations in 6-fold coordination. Similarly, for the mixed Fe/M compositions, the increase of lattice parameters from Fe to Mn and the decrease from Fe to Co/Ni are consistent. For most of the transition metals, the DFT calculations show rather regular octahedral coordination with the four equatorial bonds being systematically shorter than the two apical ones. Only the relaxed structure of the pure iron compound displays two short (2.01 Å) and two long (2.07 Å) in-plane bonds, arranged in a *trans*-configuration. Those shorter bonds alternate in-plane with the longer ones along the –(Fe–F)– corner sharing chains as depicted in Fig. 4a. In the mixed compounds this topology is not modified for iron while the other transition metals keep their more regular coordination as shown for the $Fe_{0.5}Mn_{0.5}$ case in Fig. 4b. It is interesting to note that the geometrical mismatch between the perovskite layer and the $[Bi_2O_2]$ layer is mostly accommodated by the cooperative rotation of the $[MF_6]$ octahedra around the c-axis. The magnitude of this distortion can be simply evaluated by looking at the deviation of the M–F–M angles from 180° reported in Table 2 and Fig. 5b. As expected, the larger the radius of the transition metal cation, the greater the rotation, with angles ranging from 133° for M = Mn to 144° for the smaller M = Ni.

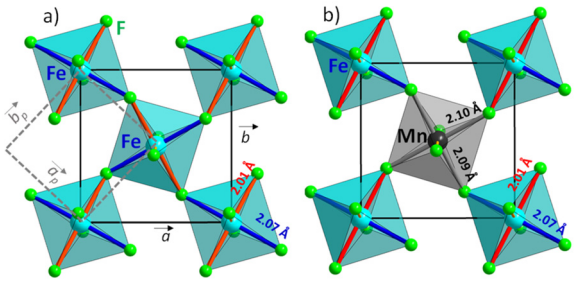

Fig. 4 $Bi_2O_2(Fe,M)F_4$. Projection along the c-axis looking at the perovskite layer of the DFT relaxed structures of (a) Fe and exemplary for a mixed-metal, the (b) $Fe_{0.5}Mn_{0.5}$ phase (blue: Fe, grey: Mn, green: F).

Evolution of the lattice parameters of the solid-solutions

Refined lattice parameters of the synthesized samples with different compositions are shown in Fig. 5c and d (numerical values are listed in Tables S2–S5). For the Rietveld refinements, a and b are kept equal since the small differences are not observed by XRD. It contrasts with our fully ordered DFT models where the a/b orthorhombic split is sometimes significant and emphasizes the Fe/M random distribution in the synthesized materials. The experimental increase in lattice parameters from Fe to Mn and the decrease from Fe to Co or Ni are consistent with theory and expectations. However, the curvatures of the main driving lines, according to Vegard's law, highlight the tilting of octahedra which are on the move during the substitution. The small in-plane change between Fe and Co is observed as well. The distribution of lattice parameters for a single target composition can be understood on the same basis as in the parent $Bi_{2-x}O_2FeF_4$ case, *i.e.*, sizable

 This journal is © The Royal Society of Chemistry 2025

Open Access Article. Published on 22 Liiqen 2025. Downloaded on 09/12/2025 6:56:30 AM.
This article is licensed under a Creative Commons Attribution-NonCommercial 3.0 Unported Licence.

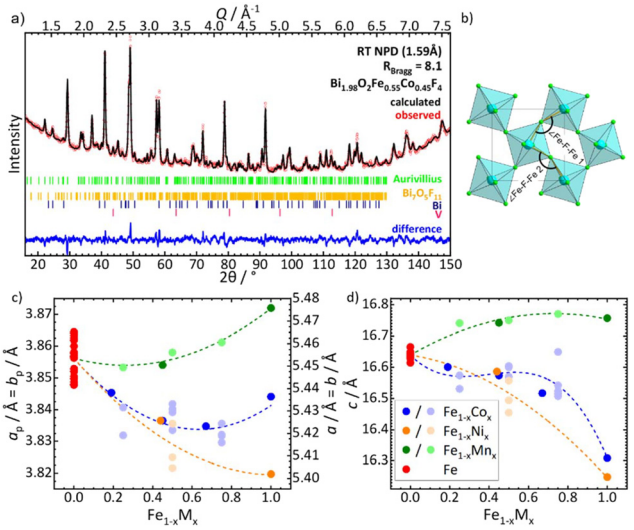

Fig. 5 (a) $Bi_2O_2Fe_{0.5}Co_{0.5}F_4$. Rietveld refinement of the high-resolution neutron diffractogram (D2B, λ = 1.59 Å) taken from a combined refinement including X-ray and neutron data of the same sample. The sample has a purity of 96 wt% with 2 wt% of $Bi_7O_5F_{11}$ and Bi each. (b) Picture of the structure depicting the M–F–M angles used to describe octahedral tilting. (c) and (d) $Bi_2O_2Fe_{1-x}M_xF_4$. Refined lattice parameters for the synthesized batches (red: Fe, green: Fe/Mn, blue: Fe/Co, orange: Fe/Ni). *a* is kept equal to *b* for all refinements. a_p and b_p indicate the lattice parameters in an ideal *I*4/*mmm* space group while *a* and *b* are given for the $P2_1ab$ group ($a = \sqrt{2}\cdot a_p$). The compositions (*x* values) are assumed from the syntheses for the pale dots. For the saturated dots they are refined from neutron diffraction (EDX for $Fe_{1-x}Ni_x$). The spread of values shows inhomogeneity in between different samples. The dashed curves are only used to highlight the trends.

concentration of various types of possible defects. In addition, it is clear that in solvothermal synthesis, fine variations between the Fe to M ratios are at play, which is confirmed by our local EDX results discussed in the ED part of the paper.

Structural NPD analysis

Owing to the difference in neutron scattering lengths of the various atoms in the structures, nuclear structure refinement of the NPD patterns at room temperature provides much more accurate data than X-ray diffraction, especially regarding the position of O/F atoms and the transition metal ratios. However, O/F and Fe/Ni contrasts are still very low. The quality of the diagrams is strongly affected by the impurities, especially the various hydrated iron fluorides and hydroxides that add an important background contribution due to the incoherent scattering of hydrogen atoms. Moreover, in the case of $Fe_{0.5}Ni_{0.5}$, an unknown impurity prevented accurate structure refinement due to intensity overlap.

A typical NPD refinement is shown in Fig. 5a for the $Fe_{0.5}Co_{0.5}$ targeted composition. Overall, we used the $P2_1ab$ Fe-model, with the additional $a = b$ constraint for stability of the refinement, since the split – if any – cannot be resolved experimentally. Besides the refinement of the Fe/M ratio and octahedral tilts, relaxing the Bi and F occupancies may help the convergence. However, these results should be considered with care due to the quality of our samples, and large correlation between anionic occupancies and thermal parameters. Table 3 lists the resulting compositions, lattice parameters and R_{Bragg} values of the various measured compounds assuming an ideal stoichiometry of the fluorite $[(Fe,M)_1F_4]$ blocks. The value of the M–F–M angles (see Fig. 5b) are also reported as measurement of the octahedra rotation. Other refinements with higher amounts of impurities are shown in Fig. S2.

The single Fe, mixed Fe/Co and Fe/Mn compounds show Bi vacancies between ~1 and ~10% as in our previous work.[8] It suggests that bismuth vacancies are a robust mechanism compensating the mixed-valence $Fe^{\sim 2.5+}$ oxidation state. However, the Bi vacancy concentration does not seem correlated to the amount of iron in the structure and we do not discard Mössbauer data for the mixed Fe/M compounds. This will be further investigated in the future after preparation of samples with sufficient purity.

The values of the ∠M–F–M angles can be compared to the values obtained on the relaxed DFT structures (Table 2). The lower distortion-amplitudes observed using NPD are probably a consequence of the disorder on the transition metal site as opposed to the artificial ordering used in the DFT calculations.

Table 3 $Bi_{2-y}O_2Fe_{1-x}M_xF_4$. Refined composition, lattice parameters, and R_{Bragg} of the Aurivillius phase of different samples retrieved from combined neutron and X-ray data Rietveld refinements. The M–F–M angles give a measure of the rotation of the octahedra in the perovskite layer (see Fig. 5b). Magnetic structures are refined against difference neutron data. The Fe/Ni ratio is determined by EDX due to similar neutron scattering lengths

Composition	∠M–F–M mag. space gr.	*a*,*b* M_x	*c* M_y	M_z	M_{tot}	R_{Bragg} R_{magn}
$Bi_{1.94}O_2FeF_4$	135°/158°	5.45890(13) Å		16.6326(6) Å		10.9
	$P2_1ab$	2.8(1)μ_B	0	3.84(8)μ_B	4.76(8)μ_B	11.2
$Bi_{1.93}O_2Fe_{0.81}Co_{0.19}F_4$	145°/153°	5.43831(7) Å		16.5999(4) Å		9.8
	$P2_1ab$	0	0	3.60(2)μ_B	3.60(2)μ_B	8.5
$Bi_{1.98}O_2Fe_{0.55}Co_{0.45}F_4$	146°/155°	5.42575(6) Å		16.5743(3) Å		8.3
	$P2_1ab$	0	0	3.16(3)μ_B	3.16(3)μ_B	14.3
$Bi_{1.95}O_2Fe_{0.33}Co_{0.67}F_4$	150°/156°	5.42313(10) Å		16.5156(5) Å		8.0
	$P2_1'ab'$	2.61(5)μ_B	0	3.30(5)μ_B	3.30(5)μ_B	22.0
$(Bi_2O_2Fe_{0.56}Ni_{0.44}F_4)$	133°/153°	5.4246(3) Å		16.5851(13) Å		15.0
	$P2_1ab$	0	0	4.09(5)μ_B	4.09(5)μ_B	17.2
$Bi_{1.86}O_2Fe_{0.55}Mn_{0.45}F_4$	153°/157°	5.44469(19) Å		16.7278(8) Å		10.7
	$P2_1ab$	0	0	2.77(2)μ_B	2.77(2)μ_B	13.2

Open Access Article. Published on 22 Liiqen 2025. Downloaded on 09/12/2025 6:56:30 AM.
This article is licensed under a Creative Commons Attribution-NonCommercial 3.0 Unported Licence.

The general trend of the evolution of the M–F–M angles, as previously described on the DFT relaxed structures, *i.e.* smaller angles are observed for the bigger cations, is not clearly observed in the experimental set, especially the Fe/Mn compound which exhibits larger M–F–M angles despite being the larger cation (Table 3). However, differently from the perfectly ordered structures used in DFT, maintaining very symmetric [MF_6] octahedra, the refined atomic coordinates show much more distorted coordination polyhedra, as seen in the variation of the two M–F–M angles reported. Although, it is difficult to be certain given the limitation of our experimental datasets, we propose that the cooperative distortion observed by DFT, giving clear distinction between the *a* and *b* cell parameters even in the case of the pure metal compositions, cannot propagate to long distances in actual materials. The resulting disorder is probably the main driver that locks $a = b$ for the experimental structures and what makes the description of the anionic lattice of these compounds so challenging.

Magnetic ordering

Table 2 gives the in-plane and interplanar magnetic exchanges (J) calculated using DFT. We note that for several mixed Fe/M ideally-ordered compounds, at least one spin-polarized configuration did not converge properly. In the single Co compound, the exchanges were found to be ferromagnetic (FM) which contradicts the experimental results. It is reminiscent of what was found by GGA+U in a previous work[9] where only LDA+U allowed for an antiferromagnetic (AFM) ground state. Finally, in the other cases one can only deduce prominent in-plane AFM exchanges in a nearly 2D magnetic topology. The large AFM J_{intra} exchange (~86 K, U = 4 eV) found for the Ni compound is in tune with our previous results (~55 K, U = 3 eV). It emphasizes that for Ni^{2+} (d^8, S = 1, $t_{2g}^6e_g^2$), the AFM contribution by e_g electrons is only improved. It suggests that for other cations, the t_{2g} electrons offer additional contributions to the total exchange (by delocalization or correlation), which may be ferromagnetic because they decrease the global AFM contribution.

The most representative magnetic susceptibility measurements for the different Fe/M solid solutions are shown in Fig. 6a. Curie–Weiss (CW) fitting to the paramagnetic regions resulted in expected moments close to those expected in a spin-only approximation (see Fig. S3). As the magnetization was corrected by adjusting the mass of the samples, subtracting the mass percentages of diamagnetic impurities for each measurement, the CW parameters should be considered with caution. Indeed, after their quantification by Rietveld refinements, some weak XRD peaks sometimes remain unassigned. Also, the linearity of the CW fitting is sometimes perturbed by small amounts of ferromagnetic impurities and it is clear that the spin-only approximation is not valid for special ions such as Co^{2+}. However, concerning the assigned magnetic impurities detailed in Table S1, their few mass percent contributions allow for minor contribution to the fitting according to Curie–Weiss laws.

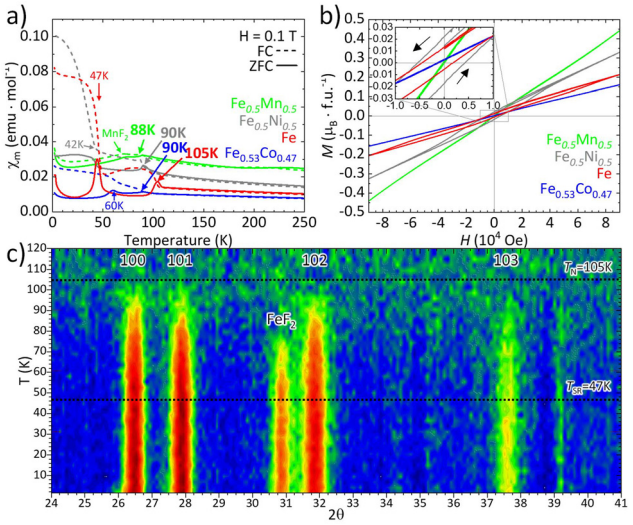

Fig. 6 $Bi_2O_2Fe_{1-x}M_xF_4$. (a) ZFC (solid lines)/FC (dotted lines) susceptibility measurements, of three mixed-metal compounds and of the parent Fe compound, at 0.1 T. (b) Magnetization *vs.* external magnetic field measurements of the same samples at 2 K. (c) $Bi_2O_2FeF_4$ indexed difference neutron diffraction patterns T–115 K (λ = 2.52 Å). The Néel temperature T_N, the spin reorientation temperature T_{SR} from the $\chi(T)$ plots are shown by dotted lines. The FeF_2-like magnetic impurity was not clearly observed by NPD.

In general, the evolution of the T_N values detected in the $\chi_m(T)$ plots matches with a monotone evolution between the end-members. As already reported for the Fe, Co, and Ni single-metal compounds, the corresponding mixed compounds show a ZFC/FC divergence below T_N. Additionally for Fe-rich samples, similarly to the Fe case, this divergence is enhanced drastically at T_{SR} (SR for spin-reorientation), as shown in Table 4. Those temperatures change with composition and match no ordering temperatures of identified impurities. The weak FM contribution is between 0.01 and 0.02μ_B/metal at 2 K, as seen from the $M(H)$ plots for selected samples shown in Fig. 6b. The weak ferromagnetic contributions are assigned to sizable spin canting compatible with Dzyaloshinskii–Moriya interactions not canceled in the $P2_1ab$ space group. However, its amplitude is not significant enough

Table 4 $(Bi_2O_2)(Fe_{1-x}M_xF_4)$: T_N and T_{SR} temperatures, effective moment μ_{eff} and Curie–Weiss temperatures Θ_{CW}. Values in brackets might have a high uncertainty since ZFC/FC divergence, indicating significant amounts of impurity, is still observed at high temperatures

Composition	T_N/K	T_{SR}/K	ZFC/FC divergence	μ_{eff}	Θ_{CW}/K
Fe	105	47	Yes	6.34	−204
$Fe_{0.81}Co_{0.19}$	100	20	Yes	4.04	−83
$Fe_{0.55}Co_{0.45}$	90	60	Yes	5.33	−244
$Fe_{0.33}Co_{0.67}$	70	—	Yes	5.57	−194
Co10	50	—	Weak	5.62	−142
$Fe_{0.5}Ni_{0.5}$	90	42	Yes	(6.15)	(−145)
$Fe_{0.75}Mn_{0.25}$	(103)	34	Yes	(2.77)	(−89)
$Fe_{0.5}Mn_{0.5}$	88	—	Weak	(5.95)	(−70)
$Fe_{0.25}Mn_{0.75}$	(35)	—	Weak	9.03	−148

This journal is © The Royal Society of Chemistry 2025

Open Access Article. Published on 22 Liiqen 2025. Downloaded on 09/12/2025 6:56:30 AM.
This article is licensed under a Creative Commons Attribution-NonCommercial 3.0 Unported Licence.

to be captured in our NPD data described below. Furthermore, at least in the parent $(Bi_{2-x}O_2)(FeF_4)$, T_{SR} is not accompanied by any significant change of its magnetic NPD pattern (see Fig. 6c). In this study, we have collected only a limited number of NPD data for the mixed Fe/M compositions such that similar "hidden" canting effects are assumed.

Low temperature neutron diffraction data have been collected on the D1B diffractometer, λ = 2.52 Å. The magnetic contributions to the diffraction patterns can be visualized by subtracting the high temperature purely nuclear pattern from the low temperature diffraction patterns. The refinements of the different patterns are shown in Fig. 7. Here, we have systematically excluded the areas corresponding to the 113 and 204 very-intense reflections, which show the most drastic effects on the difference patterns due to the lattice contraction between the two reference temperatures: 115 K and 2 K. Other excluded regions correspond to minor contributions arising from unassigned magnetically ordered impurities.

All magnetic structures can be described using a $\mathbf{k}$ = (0,0,0) propagation vector, already reported for other orthorhombic single-metal Aurivillius oxyfluorides.[8,9] Note that it is equivalent to the $\mathbf{k} = (\frac{1}{2},\frac{1}{2},0)$ propagation vector used in the Mn case,[11] treated in the $I4/mmm$ tetragonal subcell. In the assumed $P2_1ab$ space group, the a and b axes are not symmetrically equivalent but are indiscernible on powder diffraction data due to the pseudo-tetragonal ($a = b$) geometrical features. It induces a puzzling situation concerning the magnetic models in competition. To achieve homogeneity in the refined models, the plausible in-plane magnetic component was selected along the a-axis ($M_x \neq 0$, $M_y = 0$) by analogy to our

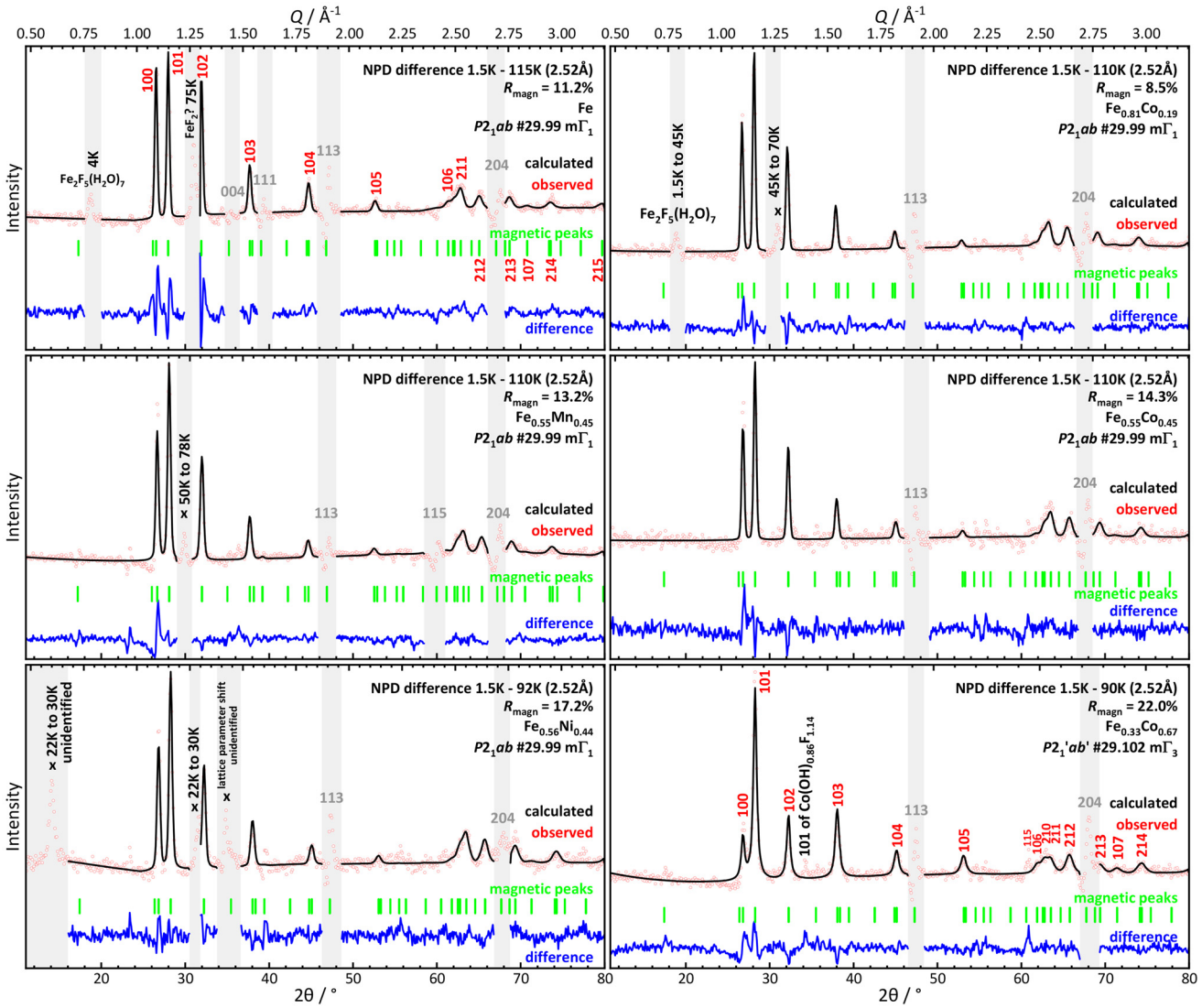

Fig. 7 $Bi_2O_2Fe_{1-x}M_xF_4$. Rietveld refinements against difference neutron data (D1B λ = 2.52 Å) of 6 measured samples of different compositions. The composition is refined in a combined Rietveld refinement including XRD and high-resolution NPD data (except for $Fe_{1-x}Ni_x$ where EDX on single particles of the powder had to be used due to similar neutron scattering lengths). For the excluded zones, *x* indicates magnetic peaks due to impurities together with their estimated appearing temperature, and grey *hkl* indices are given to artefacts due to lattice contraction.

Open Access Article. Published on 22 Liiqen 2025. Downloaded on 09/12/2025 6:56:30 AM.
This article is licensed under a Creative Commons Attribution-NonCommercial 3.0 Unported Licence.

previous published model for M = Fe and Ni.[8] After refining with our new data, the moments for the Fe sample along *a* and along *c* have slightly changed as shown in Table 3. For most of the compositions, following this, the magnetic structures are well described using the mΓ_1 mode (x, y, z: M_x, M_y, M_z; $x + 1/2$, $-y$, $-z$: M_x, $-M_y$, $-M_z$; x, $y + 1/2$, $-z$: $-M_x$, $-M_y$, M_z; $x + 1/2$, $-y + 1/2$, z :$-M_x$, M_y, $-M_z$). It leads to the magnetic space group $P2_1ab$ ($Pca2_1$ #29.99). Finally, one refined moment M_z with moments antiferromagnetically ordered parallel to the *c*-axis is sufficient to describe the measured intensities. However, within the Fe/Co solid solution, for the Co-rich composition $Bi_2O_2Fe_{0.33}Co_{0.67}F_4$ shown in Fig. 7 we observe a drastic change in the relative intensities of the magnetic peaks; see for instance the 100/101/102 reflections. Here the refinement requires switching to the mΓ_3 (x, y, z: M_x, M_y, M_z; $x + 1/2$, $-y$, $-z$: $-M_x$, M_y, M_z; x, $y + 1/2$, $-z$: M_x, M_y, $-M_z$; $x + 1/2$, $-y + 1/2$, z: $-M_x$, M_y, $-M_z$) mode and requires a mixed M_x, M_z contribution. It results in the magnetic space group $P2_1'ab'$ ($Pca'2_1'$ #29.102). This differs from the pure Fe/Co compounds[8,9] where the tilted/in-plane moments originate from the mΓ_1/mΓ_2 irreducible representations respectively. For this same Co-rich phase only, a weak contribution on the (002) peak (Q = 0.76 Å^{-1}) is observed on the magnetic NPD pattern. Its magnetic origin is uncertain, or could also concern a secondary phase. However, we note that it fits to a significant FM contribution $M_y = 0.41(7)\mu_B$ (R_{magn} = 17.5) allowed in the magnetic space group 29.102. This ferromagnetic moment is largely above the value observed for this sample on the $M(H)$

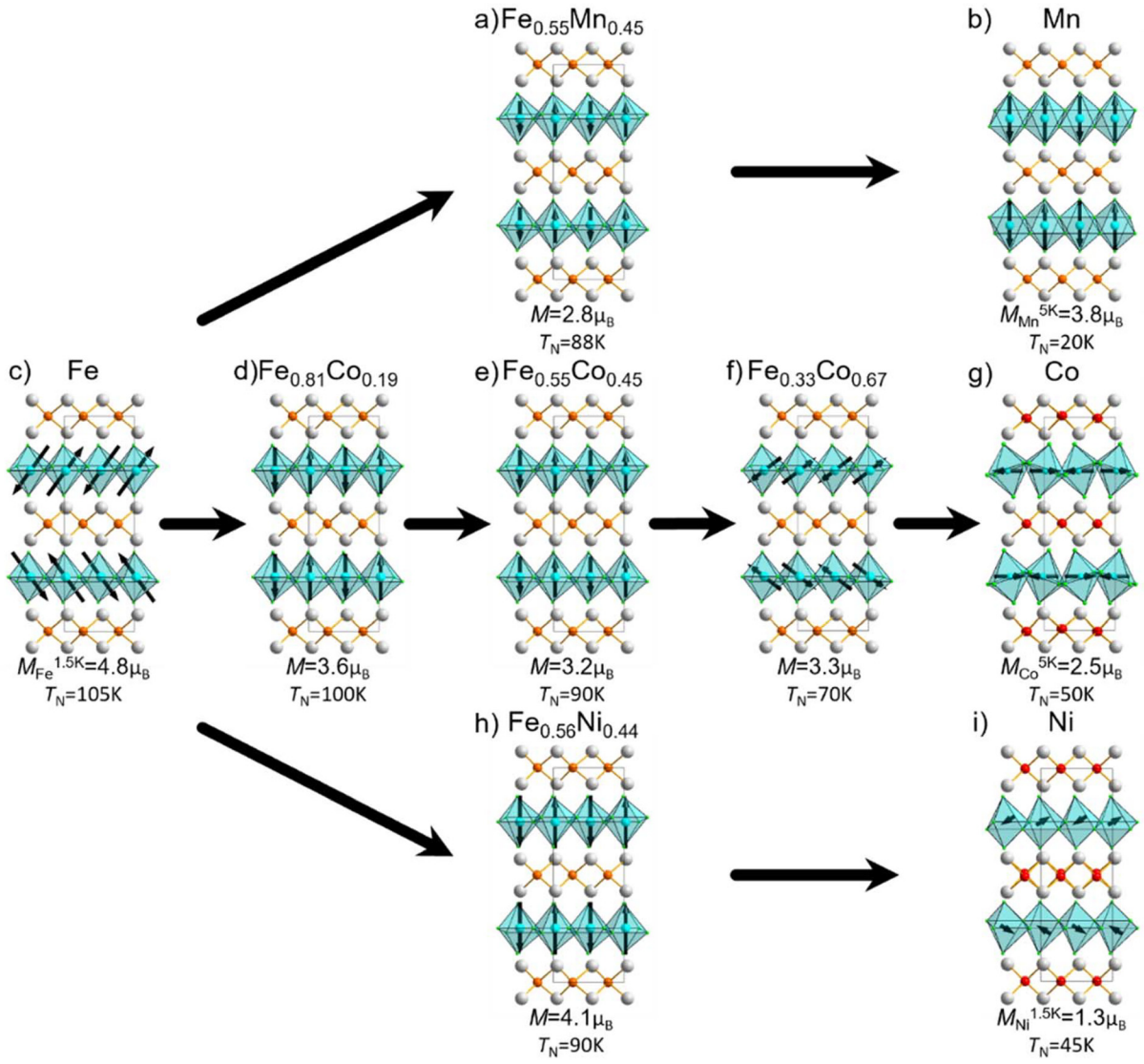

Fig. 8 $Bi_2O_2Fe_{1-x}M_xF_4$. Comparison of the refined magnetic structures from refinements against difference neutron data for 6 measured samples of different compositions and the 3 single-metal phases Mn,[11] Co,[9] and Ni[8] taken from the literature (Figures show the *ac*-plane for all compounds except for Co for which the *bc*-plane is shown). For the mixed-metal compositions, the nuclear structure ($P2_1ab$) of the parent Fe member is shown. For Mn, an arbitrary tilting scheme of the octahedra is chosen to match the other phases.

 This journal is © The Royal Society of Chemistry 2025

Open Access Article. Published on 22 Liiqen 2025. Downloaded on 09/12/2025 6:56:30 AM.
This article is licensed under a Creative Commons Attribution-NonCommercial 3.0 Unported Licence.

plot at 2 K, $M = 0.016\mu_B$ per metal. In addition, due to the low statistics of the data, the origin of this maximum remains highly uncertain.

Our final refined moments are given in Table 3 and the magnetic structures are shown in Fig. 8, including those of the single M ions for M = Fe, Co, Mn and Ni. It appears that the magnetocrystalline anisotropy driving differently each Fe, Co, and Ni parent magnetic ordering is lost after Fe/M mixing, where the spins align along the *c*-axis. Keeping in mind that this solution is the one adopted for the Heisenberg Mn^{2+} spins ($L = 0$). Then a plausible scenario would consist of the orbital component M_{SOC} not ordering, evidenced by the moments specific axial orientation in the disordered Fe/M mixed phases, and the order is only governed by M_{spin}. Following this idea, an exception is expected for the Co^{2+} case, where the SOC is prominent such that it is not fully canceled. At least the evolution of the amplitude of the refined magnetic moments validates that, after Fe/M mixing, their major contributions fully order together in spite of the cationic random distribution, far from a spin-glassy situation. Despite the change of magnetic symmetry highlighted above in the Fe/Co solid solution, we note that comparing the single layer of the Fe and $Fe_{0.33}Co_{0.67}$ compounds, the spins are oriented similarly (see Fig. 8c and f).

Even though the neutron diffraction study of mixed M^{2+} transition metals is not so well documented, the competition between highly anisotropic Fe^{2+}/Co^{2+} and Ni^{2+}/Mn^{2+} ions has been already reported in $M_xNi_{1-x}Br_2$ (M = Fe, Mn)[30] and $Mn_xCo_{1-x}O$[31] with similar reorientation of the magnetically ordered spin component at critical concentrations.

Conclusions

We found total miscibility of substituted Mn, Ni, and Co divalent cations in the parent $(Bi_{2-x}O_2)(FeF_4)$ Aurivillius oxyfluoride, after synthesis under hydrothermal conditions. Our syntheses are systematically accompanied by various secondary phases but contain only a unique Aurivillius phase per batch. However, the dispersion of the refined lattice parameters around each targeted composition emphasizes the difficulty to control the final stoichiometry and the occurrence of various possible compositional defects in the final products. At least, it is clear that the mapping of thin parts of the crystals by TEM-EDX analyses validates inhomogeneous Fe/M compositions around the NPD refined ones. Despite this apparent bulk disorder, we observed, by SAED and NPD, evidence of supercell spots which validate the ordering of the F^- anions within the perovskite sub-units, which justifies the occurrence of an orthorhombic, ordered scheme of tilted octahedra, rather than the fully disordered tetragonal subcell. It occurs independent of the Fe/M ionic size mismatch. Moreover, the spin-glass like magnetic state often observed in such mixed-cation solid solutions is not attained here. In contrast, all the prepared compounds are magnetically ordered but without the non-colinear magnetic structures adopted by the single-metal (Fe, Co, and Ni) parent phases. Instead, their refined magnetic structures highlight AFM collinear spin arrangements with moments aligned parallel to the *c*-axis, similar to the structure observed for $(Bi_2O_2)(MnF_4)$, for which the orbital contribution is non-existent due to the Mn^{2+} ions ($L = 0$). Therefore, the driving-role of the spin orbit coupling seems to be quenched in the Fe/M solid solutions due to cation disorder. Finally, the possibility is tempting that both the conservation of a main anionic and magnetic ordering in such randomly distributed Fe/M layers is enhanced by the 2D character of the weakly interacting perovskite slabs, chemically promoted by the preference for $[Bi_2O_2]$ layers, and magnetically preserving a cooperative set of coplanar Fe–Fe, Fe–M and M–M interactions, which order AFM, but would be probably lost in a glassy-regime in a 3D counterpart.

Conflicts of interest

No conflicts of interest to declare.

Data availability

Neutron diffraction data can be accessed using **https://doi.org/10.5291/ILL-DATA.5-31-3019**. The supplementary information contain details concerning the synthesis conditions of the different presented samples, refined lattice parameters and compositions, plots of the RT X-ray and neutron refinements, and susceptibility measurements. Additionally, the irreducible representations used for the magnetic refinements are given in a table for better readability. Supplementary information is available. See DOI: **https://doi.org/10.1039/d5dt01303h**.

Acknowledgements

The Fonds Européen de Développement Régional, CNRS, Région Hauts-de-France, and Ministère de l'Education Nationale de l'Enseignement Supérieur et de la Recherche are acknowledged for the funding of the X-ray diffractometer and PPMS system. For one of the samples a MPMS3 in the Institut Néel has been used for the suceptibility measurement. The Région Hauts-de-France and ILL supported the funding of J. W.'s PhD thesis. Laurence Burylo (XRD) and Delphine Filipiak (synthesis) are thanked for their help with experiments. Beam time granted at the ESRF and at the ILL is appreciated as well. The Mésocentre de calcul de Lille is thanked for the possible DFT calculations.

References

1 B. Aurivillius, *Ark. Kemi.*, 1952, **4**, 39–47.
2 A. V. Akopjan, T. V. Serov, V. A. Dolgikh, E. I. Ardaschnikova and P. Lightfoot, *J. Mater. Chem.*, 2002, **12**, 1490–1494.

Open Access Article. Published on 22 Liiqen 2025. Downloaded on 09/12/2025 6:56:30 AM.
This article is licensed under a Creative Commons Attribution-NonCommercial 3.0 Unported Licence.

3 R. L. Needs, S. E. Dann, M. T. Weller, J. C. Cherryman and R. K. Harris, *J. Mater. Chem.*, 2005, **15**, 2399–2407.
4 A. T. Giddings, E. A. S. Scott, M. C. Stennett, D. C. Apperley, C. Greaves, N. C. Hyatt and E. E. McCabe, *Inorg. Chem.*, 2021, **60**, 14105–14115.
5 I. H. Ismailzade and J. Ravez, *Ferroelectrics*, 1978, **21**, 423–424.
6 J. Chen, H. Liu, L. Zhu, Z. Fu and Y. Lu, *J. Alloys Compd.*, 2021, **873**, 159847.
7 T. Katayama, A. Chikamatsu and M. Hirayama, *Adv. Funct. Mater.*, 2025, 2500489.
8 O. Mentré, M. A. Juárez-Rosete, M. Colmont, C. Ritter, F. Fauth, M. Duttine, M. Huvé, C. Terryn, V. Duffort and Á. M. Arévalo-López, *Chem. Mater.*, 2022, **34**, 5706–5716.
9 E. A. S. Scott, E. Mitoudi Vagourdi, M. Johnsson, V. Cascos, F. John, D. Pickup, A. V. Chadwick, H. Djani, E. Bousquet, W. Zhang, P. S. Halasyamani and E. E. McCabe, *Chem. Mater.*, 2022, **34**, 9775–9785.
10 E. Mitoudi Vagourdi, S. Müllner, P. Lemmens, R. K. Kremer and M. Johnsson, *Inorg. Chem.*, 2018, **57**, 9115–9121.
11 J. Wolber, V. Duffort, D. Filipiak, X. Rocquefelte, M. Huvé, T. Famprikis, Á.-M. Arévalo-López, O. Fabelo and O. Mentré, *Chem. Mater.*, 2025, **37**(15), 5846–5856.
12 Y. Ma, X. M. Chen and Y. Q. Lin, *J. Appl. Phys.*, 2008, **103**, 124111.
13 K. Ramesha, A. Llobet, T. Proffen, C. R. Serrao and C. N. R. Rao, *J. Phys.: Condens. Matter*, 2007, **19**, 102202.
14 J. Mao, Y. Sui, X. Zhang, Y. Su, X. Wang, Z. Liu, Y. Wang, R. Zhu, Y. Wang, W. Liu and J. Tang, *Appl. Phys. Lett.*, 2011, **98**, 192510.
15 J. Rodríguez-Carvajal, *Physica B: Condens. Matter*, 1993, **192**, 55–69.
16 H. T. Stokes, D. M. Hatch and B. J. Campbell, *ISOCIF, ISOTROPY Software Suite*, iso.byu.edu.
17 WinNormos-for-Igor, WaveMetrics Inc., Wissenschaftliche Elektronik GmbH, 2008.
18 G. Kresse and J. Furthmüller, *Comput. Mater. Sci.*, 1996, **6**, 15–50.
19 G. Kresse and J. Hafner, *Phys. Rev. B:Condens. Matter Mater. Phys.*, 1994, **49**, 14251–14269.
20 G. Kresse and J. Furthmüller, *Phys. Rev. B:Condens. Matter Mater. Phys.*, 1996, **54**, 11169–11186.
21 J. P. Perdew, K. Burke and M. Ernzerhof, *Phys. Rev. Lett.*, 1996, **77**, 3865–3868.
22 P. E. Blöchl, *Phys. Rev. B:Condens. Matter Mater. Phys.*, 1994, **50**, 17953–17979.
23 S. L. Dudarev, G. A. Botton, S. Y. Savrasov, C. J. Humphreys and A. P. Sutton, *Phys. Rev. B:Condens. Matter Mater. Phys.*, 1998, **57**, 1505–1509.
24 H. J. Monkhorst and J. D. Pack, *Phys. Rev. B*, 1976, **13**, 5188–5192.
25 D. Khomskii, *Physics*, 2009, **2**, 20.
26 H. Miyamoto, T. Shinjo, Y. Bando and T. Takada, *J. Phys. Soc. Jpn.*, 1967, **23**, 1421–1421.
27 D. E. Conte, L. Di Carlo, M. T. Sougrati, B. Fraisse, L. Stievano and N. Pinna, *J. Phys. Chem. C*, 2016, **120**, 23933–23943.
28 S. Ramasamy, J. Jiang, H. Gleiter, R. Birringer and U. Gonser, *Solid State Commun.*, 1990, **74**, 851–855.
29 R. D. Shannon, *Acta Crystallogr., Sect. A*, 1976, **32**, 751–767.
30 M. W. Moore and P. Day, *J. Solid State Chem.*, 1985, **59**, 23–41.
31 D. A. O. Hope and A. K. Cheetham, *J. Solid State Chem.*, 1988, **72**, 42–51.

This journal is © The Royal Society of Chemistry 2025